Mechanics of Materials 140 (2020) 103229

Contents lists available at ScienceDirect

Mechanics of Materials

journal homepage: www.elsevier.com/locate/mechmat

Research paper

Seismic attenuation and dispersion in a cracked porous medium: An effective medium model based on poroelastic linear slip conditions

Yongjia Song[a,b,*], Hengshan Hu[a], Bo Han[b]

[a] Department of Astronautic Science and Mechanics, Harbin Institute of Technology, 92 West Dazhi Street, Harbin 150001, China
[b] Department of Mathematics, Harbin Institute of Technology, 92 West Dazhi Street, Harbin 150001, China

ARTICLE INFO

Keywords:
Crack
Porous medium
Dispersion
Attenuation
Linear slip model

ABSTRACT

Mechanical and hydraulic properties of a crack can significantly affect seismic wave propagation. To explore these effects, we developed an effective medium model that describes the P-wave dispersion and attenuation in inhomogeneous porous media containing a distribution of aligned cracks. Although there are numerous theoretical models for quantifying the seismic dispersion and attenuation, some of them are restricted to low frequencies at which only effects of the wave-induced fluid flow (WIFF) are considered but the influences of elastic scattering are ignored. Others only consider crack mechanical properties without incorporating crack permeability. The others describe the crack by a thin layer with infinitely lateral extension, neglecting the crack length information. To improve the applicability of previous theoretical models and overcome some of these restrictions, we consider a crack of finite size as a porous medium having different poroelastic properties from the matrix material and use poroelastic linear slip conditions to describe the jumps in the stress and displacement across the crack. We first study the scattering of a normally incident fast-P wave by a single circular crack. Then, by combining the theoretical solution and Foldy's scattering method, we develop an effective medium model that can relate seismic characteristics to mechanical compliance and hydraulic permeability of the cracks. Finally, we perform comprehensive parametrical analysis to study the role played by different characteristics of crack on the seismic signatures. We show that the P-wave phase velocity and attenuation are sensitive to the crack mechanical properties, fluid mobility inside the crack and crack size. The findings provide deep understandings on seismic characteristics in cracked rocks and may allow for extracting these properties from seismic data.

1. Introduction

Earth's crustal rocks often contain cracks or fractures. The cracks are believed to dominate the mechanical and hydraulic properties of the rocks. Moreover, the crack orientation can reflect the geological stress history of the rock. Therefore, much attention has been paid to develop non-invasive techniques for probing cracked rocks. The method of elastic wave is widely used for detecting inhomogeneous rocks. As such, approaches to estimate the effective properties of such cracked solids have been studied extensively in the literature (e.g., O'Connell and Budiansky, 1977; Kawahara, 1992; Kawahara and Yamashita, 1992; Smyshlyaev et al., 1993; Zhao et al., 2015; Guo et al., 2018; Song et al., 2019). The effective medium models can provide simple tools to capture the overall mechanical properties of cracked rocks, and they have a wide range of applications in geological, environmental and geophysical sciences. Based on the frequency dependence of the time delay between split shear waves in VSP data and effective medium model by Chapman (2003), Maultzsch et al. (2003, Maultzsch et al. 2007) inverted crack density, crack size and crack orientations, which are very useful for hydrocarbon reservoir modelling. Moreover, the effective medium model can be used to identify fault properties (Worthington and Hudson, 2000) and earthquake double-couple source (Pearce et al., 1988).

The relationship between inhomogeneity microstructure and overall property is a classical theme in the mechanics of heterogeneous materials and it has attracted particular attention from geophysics community. The rocks of the earth's upper crust are typically porous to some extent and often contain cracks, fractures and faults. One logical means of modelling the essential features of such rocks is to use poroelasticity theory. When seismic waves propagate in such fluid-containing cracked rocks, complex interactions occur among the solid frame, pore fluid and crack. In recent decades, many theoretical models (Hudson et al., 1996; Hudson, 2000; Pointer et al., 2000; Chapman, 2003; Chapman et al., 2003), heuristic approaches (Galvin and Gurevich, 2015; Kong et al.,

* Corresponding author at: Department of Astronautic Science and Mechanics, Harbin Institute of Technology, 92 West Dazhi Street, Harbin 150001, China.
E-mail addresses: songyongjia061220110@126.com (Y. Song), hhs@hit.edu.cn (H. Hu), bohan@hit.edu.cn (B. Han).

https://doi.org/10.1016/j.mechmat.2019.103229
Received 17 July 2019; Received in revised form 31 October 2019; Accepted 31 October 2019
Available online 01 November 2019
0167-6636/

2017; Guo et al., 2018) and numerical methods (Masson and Pride, 2007; Rubino et al., 2013, 2014; Quintal et al., 2014) have been developed to investigate frequency-dependent seismic dispersion and attenuation in cracked porous rocks.

Seminal works in the area of estimation of seismic dispersion and attenuation in cracked porous rocks include the papers by Brajanovski et al. (2005, 2006), Lambert et al. (2006), Kong et al. (2013), Rubino et al. (2015) Barbosa et al. (2016, Barbosa et al., 2017), in which they modelled the cracks as thin, compliant poroelastic layers with infinitely lateral extension. It is found that the wave-induced fluid flow (WIFF, or scattered slow P wave via mode conversion at the crack faces) contributes significant velocity dispersion and attenuation when the fluid diffusion length is comparable to the crack spacing (the distance between two crack planes). The works of these authors are important because they established adequate but simple models to relate seismic dispersion and attenuation to rock mesoscopic-scale inhomogeneity. In other word, the most distinguished contribution of these works is that the layered models regard the geometry correlations and involve some crack interactions. But their works leave out the crack length information, which is particularly important for rock permeability investigation.

The first exact solution for the elastic scattering by a fluid-saturated crack in a porous medium is credited to Galvin and Gurevich (2006, Galvin and Gurevich 2007), who investigated the normal P-wave scattering by a circular fracture. Based on the scattering solution and Foldy's (1945) scattering theorem, Galvin and Gurevich (2009) developed an effective medium model to estimate P-wave dispersion in a rock containing aligned fractures. It is found that the attenuation peak occurs when the diffusion length is of the same order of the fracture radius (see also in Gurevich et al., 2009). The work of these authors is also important because it first provides a physical interpretation of wave propagation in porous media containing fractures of finite size. Galvin and Gurevich (2015) obtained full-angle seismic dispersion anisotropy by combing linear slip deformation approximation (e.g., Sayers and Kachanov, 1991; 1995; Schoenberg and Sayers, 1995) and their previous scattering solutions. Since the shear excess compliance is assumed to be equal to its static value, their anisotropy model is restricted to low frequencies at which the fracture radius is much smaller than the elastic wavelength. Fu et al. (2018) studied corresponding P-wave dispersion due to the presence of a distribution of aligned slit fractures in plane-strain situation. Very recently, Song (2017) investigated the scattering of an oblique incident plane wave of arbitrary polarization direction (P, SV and/or SH waves) by a circular fracture. However, the papers stated above are restricted to the situation that the crack-filling fluid is incompressible or the thickness of the fluid-saturated crack is infinitesimal. In many practices, the infilled fluid is compressible, in particular, when the crack is filled with a mount of gas bubbles. Guo et al. (2018) and Song et al. (2019) studied the effect of compressibility of the crack-filling fluid on wave scattering in elasticity and showed that the crack fluid compressibility significantly controls the mechanical compliance of the crack. But how the crack fluid compressibility affects the wave propagation in porous media is still not fully understood. Very recently, Guo et al. (2017a, 2017b) proposed a heuristic model to estimate seismic dispersion and attenuation for a porous medium containing aligned cracks with compressible fluid by combing Eshelby's (1957) inclusion theory and branching function method (Gurevich et al., 2009). But this model is restricted to low-frequency range within which the effects of WIFF are considered but the influences of the elastic scattering (scattering into fast P and S waves due to mode conversion) are neglected.

In some situations, rocks are often permeated by plane discontinuities that, possessing low permeability relative to the background material, may serve as barriers for fluid flow. For example, the compaction bands (Rudnicki, 2013), which are narrow, roughly planar bands, can significantly alter the flow characteristics of the formations. On one hand, oil, gas and water may be naturally occurring in the localization bands and it is desired to withdraw these fluids. On the other hand, because of the low permeability of the localization bands, they shall be used to prevent CO_2 from emitting to the atmosphere. Therefore, detection and characterization of the localization bands are also important for reservoir and environmental sciences. The common feature of the discontinuities and cracks is that they have very small aspect ratios. In the following, we shall also call these discontinuities "cracks". To our knowledge, there is no theoretical effective medium model that simultaneously relates crack-infilling elasticity and crack permeability to the effective properties of cracked fluid-saturated rocks.

To overcome previous restrictions, in this work we derive an exact solution for the elastic wave scattering by a single crack in a porous media. In particular, physical continuities and discontinuities of quantities across the crack are described by poroelastic linear slip conditions proposed by Nakagawa and Schoenberg (2007). The linear slip conditions can relate crack opening displacement to the crack parameters and hence they permit to account for the effects of crack-infilling properties on the seismic response of an individual crack. The background is assumed to be another porous solid whose properties could be different from the crack properties. Then, based on the scattering solution and Foldy's (1945) scattering theorem, we develop an effective medium model for velocity dispersion and attenuation in a fluid-saturated rock containing a distribution of aligned cracks. Special attention is devoted to exploring the effects of crack poroelastic parameters on effective wave velocity and attenuation. Three different dispersion mechanisms (i.e., WIFF, elastic scattering and Biot's global flow) are included in the wave propagation models. Core mathematical process follows the series expansion method proposed by Krenk and Schmidt (1982).

2. Scattering by a single crack

First, we consider a circular crack whose diameter $2a$ is much larger than the size of micro-scale pores of the background material. The crack is assumed to occupy the region $r \le a$, $z = 0$ in a cylindrical coordinate system (r, θ, z). The problem is to determine the scattering waves by the crack at the normal incidence of a fast P wave. In Fig. 1, we give a sketch of the crack including geometry and loading characteristics (incident and scattered waves).

In the present paper, both the crack and background material are modelled as porous media that can be described by Biot's (1962) theory of poroelasticity. Biot's theory predicts two P waves (fast-P and slow-P) and one S wave for propagating in porous media. The fast-P and S wave behave like the ordinary elastic waves in elastic solids. The slow-P wave reduces to a diffusion-type phenomenon at low frequencies. We denote the solid displacement vector by $\mathbf{u}$, the filtration displacement vector (fluid displacement relative to the solid in a reference volume unit) by $\mathbf{w}$, the total stress tensor and pore pressure by $\boldsymbol{\sigma}$ and p, respectively. The governing equations of Biot's theory can be found in Galvin and Gurevich (2009) and Song et al. (2017a, 2017b).

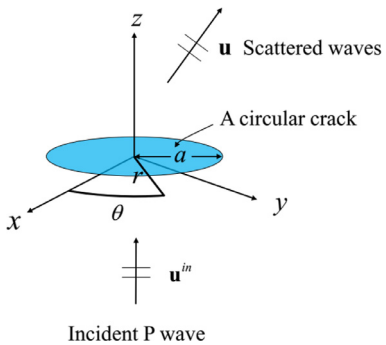

Fig. 1. A circular crack in a porous medium subjected to normally incident P wave.

In the following, we denote the physical field quantities associated with the incident wave by a superscript *in*, the scattered field quantities in the upper half space $z > 0$ by a superscript $+$, the scattered field quantities in the lower half space $z < 0$ by a superscript $-$. Throughout the paper, a time-harmonic factor $e^{-i\omega t}$, where ω is the angular frequency, t is time and i is the unit imaginary number, is suppressed. Therefore, the incident wave can be represented by the displacement vector

$$\mathbf{u}^{in} = u_0 \exp(ik_{pf} z)\hat{\mathbf{z}}, \tag{1}$$

where $\mathbf{u}^{in}$ is the incident solid displacement vector, u_0 is the amplitude, $\hat{\mathbf{z}}$ is the unit vector in the z direction and k_{pf} is the fast-P wavenumber.

2.1. Boundary conditions

According to poroelastic linear slip model proposed by Nakagawa and Schoenberg (2007), the jumps and continuities of physical quantities across a crack can be related to the crack parameters via the following explicit relations

$$u_z^+ - u_z^- = \eta_{N_D}\left\{[1 - \alpha\tilde{B}(1-\Pi)](\sigma_{zz}^- + \sigma_{zz}^{in}) + \alpha\Pi\frac{p^+ + p^- + 2p^{in}}{2}\right\} \quad (0 \le r \le a, z = 0), \tag{2}$$

$$w_z^+ - w_z^- = \alpha\eta_{N_D}\Pi\left[-(\sigma_{zz}^- + \sigma_{zz}^{in}) - \frac{1}{\tilde{B}}\frac{p^+ + p^- + 2p^{in}}{2}\right](0 \le r \le a, z = 0), \tag{3}$$

$$u_r^+ - u_r^- = \eta_T(\sigma_{rz}^- + \sigma_{rz}^{in})(0 \le r \le a, z = 0), \tag{4}$$

$$-p^+ + p^- = (-i\omega)\frac{\eta_f \Pi}{\hat{\kappa}(\omega)}\frac{w_z^+ + w_z^- + 2w_z^{in}}{2}(0 \le r \le a, z = 0), \tag{5}$$

$$\sigma_{zz}^+ = \sigma_{zz}^-(0 \le r \le a, z = 0), \tag{6}$$

$$\sigma_{rz}^+ = \sigma_{rz}^-(0 \le r \le a, z = 0), \tag{7}$$

where α is the Biot-Willis coefficient, $\tilde{B}$ is a Skempton coefficient-like parameter which is defined as $\tilde{B} = \frac{\alpha M}{H_U}$ where M is the storage modulus, H_U is the undrained P-wave modulus. $\eta_T = \frac{h}{\mu}$ and $\eta_{N_D} = \frac{h}{H_D}$ are shear and drained normal compliances of the crack. h is the crack thickness, H_D and μ are the drained P-wave modulus and the shear modulus of the crack. H_D is related to the crack frame bulk modulus K_D via the relation $H_D = K_D + \frac{4}{3}\mu$. The membrane permeability $\hat{\kappa}(\omega)$ is related to the frequency-dependent dynamic permeability $k(\omega)$ (Johnson et al., 1987) through the relation $\hat{\kappa}(\omega) = \frac{k(\omega)}{h}$. η_f is the crack fluid viscosity. The dimensionless function Π is defined as (Nakagawa and Schoenberg, 2007)

$$\Pi = \frac{\tanh\varepsilon}{\varepsilon}, \varepsilon = (1 - i)\frac{h}{2}\sqrt{\frac{\omega}{2D}}, \tag{8}$$

where $D = \frac{k_0}{\eta_f}\frac{MH_D}{H_U}$ is the diffusion coefficient, k_0 is the static permeability. Π is complex and called a "fluid-pressure dissipation factor", which approaches unity for the low-frequency limit (drained response) and approaches zero for the high-frequency limit (undrained response).

According to (Deresiewicz and Skalak, 1963), the continuity conditions of displacement, stress and pore pressure on $z = 0$ and $r > a$ can be written as

$$u_z^+ = u_z^-(r > a, z = 0), \tag{9}$$

$$w_z^+ = w_z^-(r > a, z = 0), \tag{10}$$

$$u_r^+ = u_r^-(r > a, z = 0), \tag{11}$$

$$p^+ = p^-(r > a, z = 0), \tag{12}$$

$$\sigma_{zz}^+ = \sigma_{zz}^-(r > a, z = 0), \tag{13}$$

$$\sigma_{rz}^+ = \sigma_{rz}^-(r > a, z = 0). \tag{14}$$

It should be noted that the poroelastic parameters given in Eqs. (2)-(5) are associated with the crack. To differentiate the matrix (background material) parameters from the those of the crack, we will denote the matrix poroelastic parameters by a superscript B. For example, H_U^B denotes the undrained P-wave modulus of the matrix, while H_U denotes the undrained P-wave modulus of the crack.

2.2. Solutions

Because we consider a normally incident P wave, the scattered fields are axis-symmetric and independent of the azimuth angle θ. According to Song et al. (2017a), the scattered fields in the upper half space can be expressed as

$$u_z^+ = \int_0^\infty \left[A_s^+ k e^{-\eta_s z} - \sum_{i=pf}^{ps} A_i^+ \eta_i e^{-\eta_i z}\right] J_0(kr) k\mathrm{d}k, \tag{15}$$

$$w_z^+ = \int_0^\infty \left[\chi_s^B A_s^+ k e^{-\eta_s z} - \sum_{i=pf}^{ps} \chi_i^B A_i^+ \eta_i e^{-\eta_i z}\right] J_0(kr) k\mathrm{d}k, \tag{16}$$

$$u_r^+ = \int_0^\infty \left[A_s^+ \eta_s e^{-\eta_s z} - \sum_{i=pf}^{ps} A_i^+ k e^{-\eta_i z}\right] J_1(kr) k\mathrm{d}k \tag{17}$$

$$p^+ = \mu^B \int_0^\infty \left[\sum_{i=pf}^{ps} \varsigma_i^B A_i^+ k_i^2 e^{-\eta_i z}\right] J_0(kr) k\mathrm{d}k, \tag{18}$$

$$\sigma_{zz}^+ = \mu^B \int_0^\infty \left[\sum_{i=pf}^{ps} (2k^2 - \tau_i^B k_i^2) A_i^+ e^{-\eta_i z} - 2A_s^+ \eta_s k e^{-\eta_s z}\right] J_0(kr) k\mathrm{d}k, \tag{19}$$

$$\sigma_{rz}^+ = \mu^B \int_0^\infty \left[2\sum_{i=pf}^{ps} A_i^+ \eta_i k e^{-\eta_i z} - A_s^+ (2k^2 - k_s^2) e^{-\eta_s z}\right] J_1(kr) k\mathrm{d}k, \tag{20}$$

where $J_i()$ is the Bessel function of the first kind of order i, the dimensionless parameters

$$\left.\begin{aligned}\tau_i^B &= \frac{H_U^B + C^B \chi_i^B}{\mu^B} \\ \varsigma_i^B &= \frac{C^B + M^B \chi_i^B}{\mu^B}\end{aligned}\right\}(i = pf, ps), \tag{21}$$

and the quantity

$$\eta_i^2 = k^2 - k_i^2 (i = pf, ps, s). \tag{22}$$

To satisfy the radiation condition, the wavenumber $\eta_i(k)$ is subject to the following restriction:

$$\mathrm{Re}[\eta_i(k)] \ge 0 (i = pf, ps, s) \tag{23}$$

for any positive k. The symbol $k_i (i = pf, ps, s)$ denotes the wavenumber in corresponding wave mode, where the subscripts *pf, ps* and *s* refer to fast-P, slow-P and S waves, respectively. The symbol $\chi_i^B (i = pf, ps, s)$ denotes the ratio of filtration displacement to the solid displacement in corresponding wave mode. The symbol C^B denotes a modulus defined in Biot's theory, it can be related to Biot-Willis coefficient and storage modulus via the relation $C^B = \alpha^B M^B$.

The scattered fields in the lower half space can be expressed as:

$$u_z^- = \int_0^\infty \left[A_s^- k e^{\eta_s z} + \sum_{i=pf}^{ps} A_i^- \eta_i e^{\eta_i z}\right] J_0(kr) k\mathrm{d}k, \tag{24}$$

$$w_z^- = \int_0^\infty \left[\chi_s^B A_s^- k e^{\eta_s z} + \sum_{i=pf}^{ps} \chi_i^B A_i^- \eta_i e^{\eta_i z} \right] J_0(kr) k \mathrm{d}k, \tag{25}$$

$$u_r^- = \int_0^\infty \left[-A_s^- \eta_s e^{\eta_s z} - \sum_{i=pf}^{ps} A_i^- k e^{\eta_i z} \right] J_1(kr) k \mathrm{d}k, \tag{26}$$

$$p^- = \mu^B \int_0^\infty \left[\sum_{i=pf}^{ps} \varsigma_i^B A_i^- k_i^2 e^{\eta_i z} \right] J_0(kr) k \mathrm{d}k, \tag{27}$$

$$\sigma_{zz}^- = \mu^B \int_0^\infty \left[\sum_{i=pf}^{ps} (2k^2 - \tau_i^B k_i^2) A_i^- e^{\eta_i z} + 2A_s^- \eta_s k e^{\eta_s z} \right] J_0(kr) k \mathrm{d}k, \tag{28}$$

$$\sigma_{rz}^- = \mu^B \int_0^\infty \left[-2 \sum_{i=pf}^{ps} A_i^- \eta_i k e^{\eta_i z} - A_s^- (2k^2 - k_s^2) e^{\eta_s z} \right] J_1(kr) k \mathrm{d}k. \tag{29}$$

The unknown coefficients A_i^- and A_i^+ for $i = pf, ps, s$ can determined from the boundary conditions. The stress continuity conditions (6), (7), (13) and (14) immediately give

$$\left.\begin{aligned} A_s^+ + A_s^- &= \tfrac{1}{2\eta_s k} \textstyle\sum_{i=pf}^{ps} (2k^2 - \tau_i^B k_i^2)(A_i^+ - A_i^-) \\ A_s^+ - A_s^- &= \tfrac{2k}{2k^2 - k_s^2} \textstyle\sum_{i=pf}^{ps} (A_i^+ + A_i^-)\eta_i \end{aligned}\right\}. \tag{30}$$

Substitution of expressions (15)-(29) into boundary conditions (2)-(5) and (9)-(12) and then use of Eq. (30) in the results give a series of integral equations

$$\int_0^\infty \left[\sum_{i=pf}^{ps} (A_i^+ + A_i^-) f_1^i(k) \right] J_0(kr) k \mathrm{d}k = s_1 (0 \le r \le a), \tag{31}$$

$$\int_0^\infty \left[\sum_{i=pf}^{ps} (A_i^+ + A_i^-) f_2^i(k) \right] J_0(kr) k \mathrm{d}k = s_2 (0 \le r \le a), \tag{32}$$

$$\int_0^\infty \left[\sum_{i=pf}^{ps} (A_i^+ - A_i^-) f_3^i(k) \right] J_1(kr) k \mathrm{d}k = s_3 (0 \le r \le a), \tag{33}$$

$$\int_0^\infty \left[\sum_{i=pf}^{ps} (A_i^+ - A_i^-) f_4^i(k) \right] J_0(kr) k \mathrm{d}k = s_4 (0 \le r \le a), \tag{34}$$

$$\int_0^\infty \left[\frac{k_s^2}{2k^2 - k_s^2} \sum_{i=pf}^{ps} (A_i^+ + A_i^-)\eta_i \right] J_0(kr) k \mathrm{d}k = \begin{cases} 0 (r > a) \\ \Delta u_z(r) (0 \le r \le a) \end{cases}, \tag{35}$$

$$\int_0^\infty \left[\sum_{i=pf}^{ps} (A_i^+ + A_i^-) \left(\frac{2\chi_s^B k^2}{2k^2 - k_s^2} - \chi_i^B \right) \eta_i \right] J_0(kr) k \mathrm{d}k = \begin{cases} 0 (r > a) \\ \Delta w_z(r) (0 \le r \le a) \end{cases}, \tag{36}$$

$$\int_0^\infty \left[\sum_{i=pf}^{ps} \left(-\frac{\tau_i^B k_i^2}{2k} \right) (A_i^+ - A_i^-) \right] J_1(kr) k \mathrm{d}k = \begin{cases} 0 (r > a) \\ \Delta u_r(r) (0 \le r \le a) \end{cases}, \tag{37}$$

$$\mu^B \int_0^\infty \left[\sum_{i=pf}^{ps} (A_i^+ - A_i^-) \varsigma_i^B k_i^2 \right] J_0(kr) k \mathrm{d}k = \begin{cases} 0 (r > a) \\ \Delta p(r) (0 \le r \le a) \end{cases}, \tag{38}$$

where the functions $f_j^i(k)$ and s_j (j = 1, 2, ...,4) are lengthy and we thus collect their expressions in Appendix A. $\Delta u_z(r)$, $\Delta w_z(r)$, $\Delta u_r(r)$ and $\Delta p(r)$ denote the displacement and pore pressure jumps across the crack faces. They are defined as follows

$$\left.\begin{aligned} \Delta u_z(r) &= u_z^+ - u_z^- \\ \Delta w_z(r) &= w_z^+ - w_z^- \\ \Delta u_r(r) &= u_r^+ - u_r^- \\ \Delta p(r) &= p^+ - p^- \end{aligned}\right\} (0 \le r \le a, z = 0). \tag{39}$$

Now, applying the inverse Hankel transform to Eqs. (35)-(38) gives evaluation of the coefficients A_i^- and A_i^+ in terms of the displacement and pore pressure jumps on the crack faces.

$$\frac{k_s^2}{2k^2 - k_s^2} \sum_{i=pf}^{ps} (A_i^+ + A_i^-)\eta_i = \int_0^a \Delta u_z(r) J_0(kr) r \mathrm{d}r, \tag{40}$$

$$\sum_{i=pf}^{ps} \left(\frac{2\chi_s^B k^2}{2k^2 - k_s^2} - \chi_i^B \right) (A_i^+ + A_i^-)\eta_i = \int_0^a \Delta w_z(r) J_0(kr) r \mathrm{d}r, \tag{41}$$

$$\sum_{i=pf}^{ps} \left(-\frac{\tau_i^B k_i^2}{2k} \right) (A_i^+ - A_i^-) = \int_0^a \Delta u_r(r) J_1(kr) r \mathrm{d}r, \tag{42}$$

$$\mu^B \sum_{i=pf}^{ps} (A_i^+ - A_i^-) \varsigma_i^B k_i^2 = \int_0^a \Delta p(r) J_0(kr) r \mathrm{d}r. \tag{43}$$

Note that the scattering problem will be fully solved if the displacement and pore pressure discontinuities are known. To obtain the displacement and pore pressure discontinuities, we follow the Legendre series expansion method proposed by Krenk and Schmidt (1982). Realizing that the near-tip stress of a crack possesses inverse square root singularity, the displacement and pore pressure jumps can be expanded as

$$\Delta u_z(r) = 2a \sum_{l=0}^{\infty} U_l p_l^0(r), \tag{44}$$

$$\Delta w_z(r) = 2a \sum_{l=0}^{\infty} W_l p_l^0(r), \tag{45}$$

$$\Delta u_r(r) = 2a \sum_{l=0}^{\infty} U_l^r p_l^1(r), \tag{46}$$

$$\Delta p(r) = 2\mu^B \sum_{l=0}^{\infty} P_l p_l^0(r), \tag{47}$$

with

$$p_l^m(r) = -\frac{P_{m+2l+1}^m \left(\sqrt{1 - \frac{r^2}{a^2}} \right)}{P_{m+2l+1}^{m+1}(0)}, \tag{48}$$

where $P_l^m()$ is the associated Legendre function of the first kind. The inner integral in Eqs. (40)-(43) is now evaluated by use of the result (Krenk, 1982)

$$\int_0^a p_l^m(r) r J_m(kr) \mathrm{d}r = (-1)^l \frac{a}{k} j_{m+2l+1}(ka), \tag{49}$$

where $j_m()$ is the spherical Bessel function of the first kind. Thus, Eqs. (40)-(43) become

$$\frac{k_s^2}{2k^2 - k_s^2} \sum_{i=pf}^{ps} (A_i^+ + A_i^-)\eta_i = 2a^2 \sum_{l=0}^{\infty} U_l (-1)^l \frac{j_{2l+1}(ka)}{k}, \tag{50}$$

$$\sum_{i=pf}^{ps} \left(\frac{2\chi_s^B k^2}{2k^2 - k_s^2} - \chi_i^B \right) (A_i^+ + A_i^-)\eta_i = 2a^2 \sum_{l=0}^{\infty} W_l (-1)^l \frac{j_{2l+1}(ka)}{k}, \tag{51}$$

$$\sum_{i=pf}^{ps} \left(-\frac{\tau_i^B k_i^2}{2k} \right) (A_i^+ - A_i^-) = 2a^2 \sum_{l=0}^{\infty} U_l^r (-1)^l \frac{j_{2l+2}(ka)}{k}, \tag{52}$$

$$\sum_{i=pf}^{ps} (A_i^+ - A_i^-) \varsigma_i^B k_i^2 = 2a \sum_{l=0}^{\infty} P_l (-1)^l \frac{j_{2l+1}(ka)}{k}. \tag{53}$$

Multiplying both sides of the integral Eqs. (31)-(34) by $\frac{p_j^0(r)r}{a^3}$, integrating the resulting equation with respect to r from 0 to a, and introducing the relations (50)-(53) into the results, we obtain a linear system of equations for the expansion coefficients

$$\begin{cases} \sum_{l=0}^{\infty} U_l(-1)^{l+j}A_{lj} + \sum_{l=0}^{\infty} W_l(-1)^{l+j}B_{lj} = S_j^1 \\ \sum_{l=0}^{\infty} U_l(-1)^{l+j}C_{lj} + \sum_{l=0}^{\infty} W_l(-1)^{l+j}D_{lj} = S_j^2 \\ \sum_{l=0}^{\infty} U_l^r(-1)^{l+j}E_{lj} + \sum_{l=0}^{\infty} P_l(-1)^{l+j}F_{lj} = S_j^3 \\ \sum_{l=0}^{\infty} U_l^r(-1)^{l+j}G_{lj} + \sum_{l=0}^{\infty} P_l(-1)^{l+j}H_{lj} = S_j^4 \end{cases}, \tag{54}$$

and

$$\begin{cases} S_j^1 = \frac{\eta_{N_D}}{a^3}[1-\alpha\tilde{B}(1-\Pi)]\int_0^a \sigma_{zz}^{in}|_{z=0}p_j^0(r)r\mathrm{d}r + \frac{\alpha\eta_{N_D}\Pi}{a^3} \\ \qquad \int_0^a p^{in}|_{z=0}p_j^0(r)r\mathrm{d}r \\ S_j^2 = -\frac{\alpha\eta_{N_D}\Pi}{a^3}\int_0^a \sigma_{zz}^{in}|_{z=0}p_j^0(r)r\mathrm{d}r - \frac{\alpha\eta_{N_D}\Pi}{a^3\tilde{B}}\int_0^a p^{in}|_{z=0}p_j^0(r)r\mathrm{d}r, \\ S_j^3 = \frac{\eta_T}{a^3}\int_0^a \sigma_{rz}^{in}|_{z=0}p_j^1(r)r\mathrm{d}r \\ S_j^4 = -\frac{\mathrm{i}\omega\eta_f\Pi}{\mu^B a^2\hat{k}(\omega)}\int_0^a w_z^{in}|_{z=0}p_j^0(r)r\mathrm{d}r \end{cases} \tag{55}$$

where the matrices A_{lj}, B_{lj},...H_{lj} are collected in Appendix B. The coefficients S_j^1, S_j^2, S_j^3 and S_j^4 are determined by the incident wave, their explicit expressions are also given in Appendix B.

We have derived the exact solution of the scattering problem for a single crack imbedded in an infinite porous solid. Because we adopted poroelastic linear slip conditions, the solution can relate the crack poroelastic properties to the scattered waves. In next section, we will use the scattering solution to develop an effective medium model for the wave propagation in a porous rock with a set of aligned cracks.

3. A sparse distribution of aligned cracks

3.1. Effective properties of a porous material containing aligned cracks

Here, we are concerned with velocity dispersion and attenuation in a cracked porous material. We assume that the crack positions are random but the crack orientation is aligned. As shown in Fig. 2, the crack axes are parallel to z-axis. We assume that the medium contains one set of cracks which have the same radius a. For simplicity, the cracks are assumed to have the same poroelastic properties, size and aspect ratio. According to Foldy's (1945) scattering theorem, the effective P-wavenumber k_{eff} of porous material containing cracks can be expressed in terms of scattered far fields

$$k_{eff}^2 = k_{pf}^2 + 4\pi n_0 f(0), \tag{56}$$

where n_0 is the crack number density (number of cracks per unit volume) and $f(0)$ is the scattered far-field amplitude of the fast-P wave in the forward direction (with respect to the incident wave) by a single crack. Mathematically, according to Gubernatis et al. (1977), $f(0)$ is related to the scattered far field from the following equation

$$u_z^+(r=0,z) = u_0 f(0)\frac{e^{\mathrm{i}k_{pf}z}}{z}(z\to\infty), \tag{57}$$

where u_0 is the incident wave amplitude. By using the method of steepest descent (e.g., Bleistein and Handelsman, 1986) and large-argument asymptotic expansion (Olver et al., 2010) of the spherical Bessel function, we obtain

$$f(0) = \mathrm{i}\frac{\chi_{ps}^B U_0 - W_0}{\left(\chi_{pf}^B - \chi_{ps}^B\right)u_0}\frac{k_{pf}a^3}{3} + \frac{\tau_{ps}^B P_0}{\left(\tau_{ps}^B\varsigma_{pf}^B - \tau_{pf}^B\varsigma_{ps}^B\right)u_0}\frac{a^2}{3}, \tag{58}$$

where U_0, W_0 and P_0 are the expansion coefficients defined in Eq. (44), (45) and (47). Once the effective wavenumber k_{eff} is determined, the effective phase velocity v_{eff} and inverse quality factor Q^{-1} can be obtained from

$$v_{eff} = \frac{\omega}{\mathrm{Re}(k_{eff})}, \tag{59}$$

and

$$Q^{-1} = 2\frac{\mathrm{Im}(k_{eff})}{\mathrm{Re}(k_{eff})}. \tag{60}$$

The expressions (59) and (60) can be used to quantify the velocity dispersion and attenuation due to the scattering by a plane fast-P wave by randomly distributed aligned cracks. To do so, the system of linear Eq. (54) has to be solved numerically for every frequency.

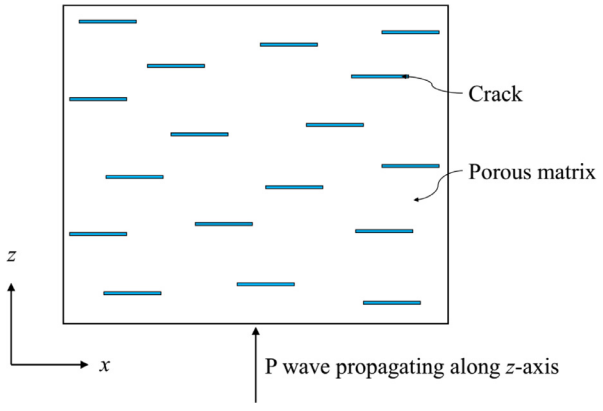

Fig. 2. P wave propagating along z-axis in a cracked porous medium.

3.2. Consistency with incompressible-crack-fluid model

We have developed an effective medium model that can relate wave characteristics to the mechanical compliance and hydraulic permeability of the cracks. It is expected that the present model can reduce to previous model (Galvin and Gurevich, 2009) of a crack containing incompressible fluid under corresponding assumptions. In the following, let us check the consistency between the present model and the incompressible-crack-fluid model.

For the incompressible-crack-fluid model, the crack space is filled with pure fluid. A key assumption is that the crack thickness is so small that the non-dimensional factor $\frac{2a}{h}\frac{K_f}{\mu^B} \gg 1$, where K_f is the bulk modulus of the crack fluid. Because the crack is thin enough and the crack faces are permeable, there is no pore pressure jump across the crack plane. These statements imply that the crack parameters can reduce to

$$\left.\begin{array}{l} \alpha = \tilde{B} = 1 \\ \eta_{N_D} = \eta_T \to \infty \end{array}\right\}. \tag{61}$$

In this case, the boundary conditions (2)-(5) directly reduce to

$$\left.\begin{array}{l} \Delta u_z + \Delta w_z = 0 \\ \sigma_{zz}^+ + \sigma_{zz}^{in} = -(p^+ + p^{in}) \\ u_r^+ = u_r^- \\ p^+ = p^- \end{array}\right\}(0 \le r \le a, z = 0) \tag{62}$$

which are the same as the boundary conditions used in Galvin and Gurevich (2009). Simultaneously, the linear system of Eq. (54) reduces to

$$\begin{cases} \sum_{l=0}^{\infty} U_l(-1)^{l+j}a_{lj} = \frac{\mathrm{i}k_{pf}u_0}{3a}\left(\tau_{pf}^B - \varsigma_{pf}^B\right)\delta_{j0}, \\ U_l + W_l = U_l^r = P_l = 0 \end{cases} \tag{63}$$

where

$$a_{lj} = \int_0^\infty \left\{ 4\frac{k^2\eta_s}{k_s^2} - \frac{2k^2\left(\chi_s^B - \chi_{ps}^B\right) + k_s^2\left(1+\chi_{ps}^B\right)}{k_s^2\left(\chi_{pf}^B - \chi_{ps}^B\right)\eta_{pf}}\left[2k^2 - \left(\tau_{pf}^B - \varsigma_{pf}^B\right)k_{pf}^2\right] \right.$$
$$\left. + \frac{2k^2\left(\chi_s^B - \chi_{pf}^B\right) + k_s^2\left(1+\chi_{pf}^B\right)}{k_s^2\left(\chi_{pf}^B - \chi_{ps}^B\right)\eta_{ps}}\left[2k^2 - \left(\tau_{ps}^B - \varsigma_{ps}^B\right)k_{ps}^2\right] \right\} \frac{1}{k} j_{2l+1}(ka) j_{2j+1}(ka)\mathrm{d}k, \tag{64}$$

Eqs. (63) and (64) are equivalent to the results obtained by Song (2017) who solved the scattering by a circular crack containing incompressible fluid by using the series expansion method. It should be noted that at the normal incidence of a fast-P wave, Song (2017)'s results agree with those of Galvin and Gurevich (2007, 2009) who, using a different method, reduced the scattering problem into a Fredholm integral equation of the second kind.

In this subsection, we have shown that how the present model reduces to the incompressible-crack-fluid model. Therefore, the present model can be regarded as an extended work of Galvin and Gurevich's (2009) model. In some sense, the consistency with the previous model validates our scattering model.

4. Examples and discussions

4.1. Parameters

Numerical results of the frequency-dependent velocity and attenuation for different crack properties and mechanistic insights on these results are given in this section. In Table 1, we list the material parameters for numerical calculations. For the purpose of exploring the effects of crack on overall effective properties, throughout subsequent numerical examples, the matrix parameters and crack density $\varepsilon = n_0 a^3 = 0.1$ are fixed. In Table 2, we show detailed choices of the crack parameters in each example.

4.2. Effects of crack fluid mobility on wave dispersion and attenuation

The ratio of material permeability to fluid viscosity coefficient defines fluid mobility (e.g., Batzle et al., 2006). The crack fluid mobility can largely control fluid flow and pore pressure and further affects the velocity dispersion and attenuation. Fig. 3 illustrates the effects of crack permeability on the phase velocity and inverse quality factor. It is shown that when the crack permeability is smaller than that of the matrix, the dispersion and attenuation due to WIFF are sensitive to the crack permeability. Specifically, in Fig. 3(a) we give the frequency-dependent P-wave phase velocities for different values of the crack permeability. It is found that in the low-frequency range ($f < 10^4$ Hz) if the crack permeability value decreases one order of magnitude, the velocity dispersion curves will roughly shift towards low frequencies by one order of magnitude.

In Fig. 3(b), we show the results of the inverse quality factor. In the low-frequency range ($f < 10^4$ Hz) the characteristic frequency of the attenuation peak also roughly moves to low-frequency range by one order of magnitude if the permeability decreases one order of magnitude. By the way, to compare the results with the dispersion and attenuation in the uncracked rock, we also display the P-wave velocity and inverse quality factor in the matrix material. Neither dispersion nor attenuation is observed in the matrix at such low frequencies, which suggests that the low-frequency dispersion and attenuation in the cracked material are attributed to the cracks. Essentially, the low-frequency velocity dispersion and attenuation in the cracked materials are caused by the mechanism of the WIFF, as the characteristic frequency of the WIFF is actually proportional to the material diffusivity which is also proportional to the fluid mobility (Müller et al., 2010).

It should be emphasized that when the crack permeability is comparable to or greater than that of the matrix, the dispersion and attenuation due to the WIFF become not sensitive to the crack permeability. The reason is that when the crack is very permeable, the crack no longer serves as a barrier to prevent fluid motion. Consequently, the fluid will have enough time to flow into the matrix during each oscillatory compressional half-cycle.

For all cases of non-zero values of the crack permeability, the low-frequency limits of the P-wave velocity are independent of the crack permeability. This is due to the fact that, in the low-frequency limit (or at statics) the fluid pressure is in equilibrium between the pores and cracks and all velocity curves converge to the same value. We also see that for the impermeable crack (i.e., the crack permeability $k_0 = 0$), the low-frequency limit of the P-wave velocity is greater than that of a permeable (or partially permeable) crack. This phenomenon can be explained as follows. For $k_0 = 0$, the crack is hydraulically isolated from the matrix pores so that no fluid mass exchange occurs between the cracks and surrounding pores. As a result, when a P-wave propagates in such a material, both cracks and matrix behave as undrained media. Even in low-frequency range, unrelaxed fluid pressure can be induced, resulting in larger velocity than the case of a permeable crack.

An important result of the impermeable crack situation is that its low-frequency velocity provides us an upper bound to quantify the dispersion magnitude between the low-frequency limit and the no-flow limit. Typically, Fig. 3(a) shows that for frequency $f < 10^4$ Hz, as the frequency increases, most of the velocity curves converge to the result of impermeable crack.

In Fig. 3(b), we also find that for frequency $f < 10^4$ Hz the magnitude of the first attenuation peak (which is caused by the WIFF) is not sensitive to the crack permeability and remains almost unchanged at small values of the crack permeability. In contrast, for large values of the crack permeability, the magnitude of the first attenuation peak tends to

Table 1
Poroelastic parameters used for the numerical examples. .

Matrix property	Symbol	Value	Crack property	Symbol	Value
Static permeability	k_0^B	0.01D	Static permeability	k_0	1D[a]
Frame bulk modulus	K_D^B	26 GPa	Frame bulk modulus	K_D	0.52 GPa
Frame shear modulus	μ^B	31 GPa	Frame shear modulus	μ	0.62 GPa
Fluid bulk modulus	K_f^B	2.25 GPa	Fluid bulk modulus	K_f	2.25 GPa
Fluid viscosity	η_f^B	10^{-3} Pa•s	Fluid viscosity	η_f	10^{-3} Pa•s
Solid bulk modulus		36 GPa	Solid bulk modulus		36 GPa
Porosity		0.1	Porosity		0.5
Tortuosity		3	Tortuosity		1
Fluid density		1000 kg/m^3	Fluid density		1000 kg/m^3
Solid density		2600 kg/m^3	Crack radius	a	0.5 m
			Crack thickness	h	10^{-3} m

Notice that some parameters are not noted by symbols since they are not referred to, but they are necessary for numerical calculation.
[a] 1D $\approx 1.0 \times 10^{-12}$ m^2.

Table 2
Crack parameter choice for calculating the velocity and attenuation.

Result	Varying property	Symbol	Values of the varying property	Other properties
Fig. 3	Static permeability	k_0	0–∞	Shown in Table 1
Fig. 4	Fluid viscosity	η_f	10^{-3}–10^{4} Pa•s	Shown in Table 1
Fig. 5	Frame bulk modulus	K_D	0–5 GPa	Shown in Table 1
Fig. 6	Fluid bulk modulus	K_f	0.01–5 GPa	Shown in Table 1
Fig. 7	Crack size	a, h	a = =0.15–50 m, h/a = =0.002	Shown in Table 1

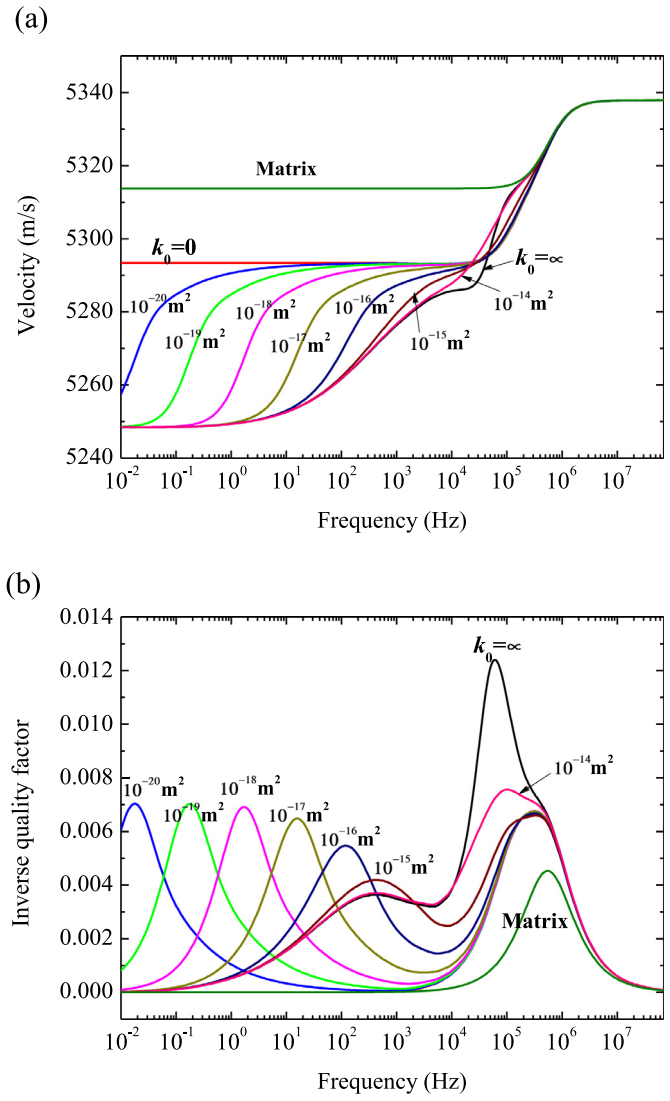

Fig. 3. P-wave phase velocity (a) and inverse quality factor (b) versus frequency for different crack permeability values. .

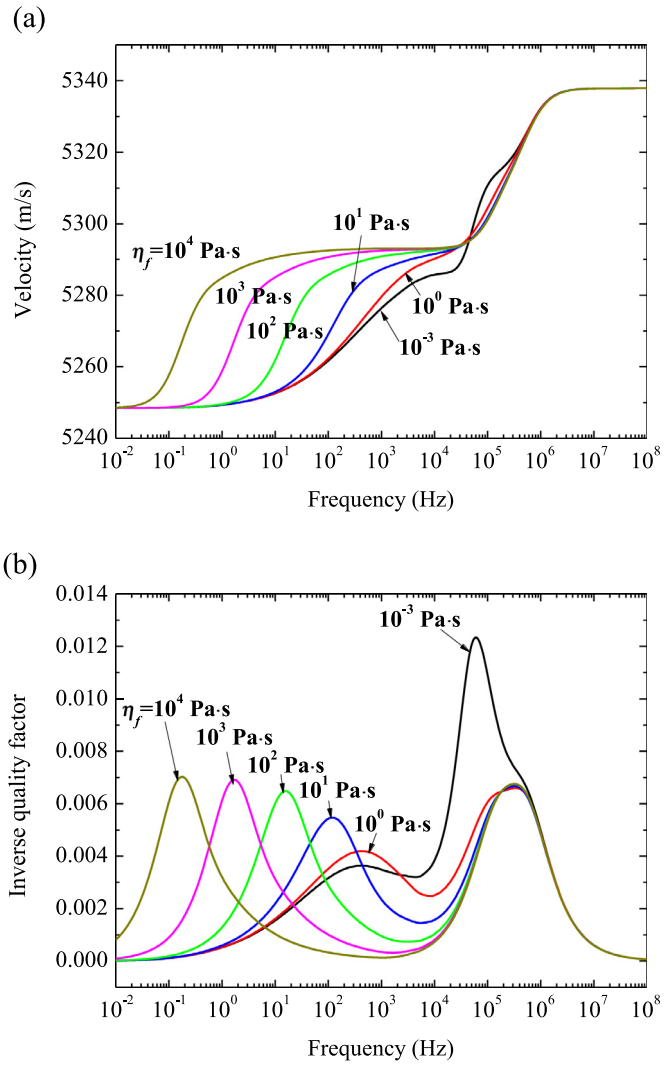

Fig. 4. P-wave phase velocity (a) and inverse quality factor (b) versus frequency for different crack fluid viscosity values.

decrease with the increase of crack permeability. This result indicates that the characteristic frequency of the WIFF moves to higher frequency at which the effects of elastic scattering become important and the effects of WIFF and elastic scattering compete with each other at certain frequencies.

At frequencies $10^4 < f < 3 \times 10^5$Hz, we find the second attenuation peak in Fig. 3(b). Such intermediate-frequency (or the second) attenuation peak is attributed to elastic scattering. Correspondingly, in Fig. 3(a) we can find velocity dispersion due to elastic scattering within such frequency range. It is shown that the velocity dispersion due to elastic scattering is constrained between the no-flow limit and the uncracked limit. For frequency $f > 3 \times 10^5$ Hz, all velocity and attenuation curves converge to those of the uncracked matrix. Note that in such high-frequency range there still exist velocity dispersion and attenuation. It turns out that the high-frequency (or the third) dispersion and attenuation are produced by Biot's global flow.

Fig. 4 shows the velocity and inverse quality factor for different crack fluid viscosities. By comparing these dispersion and attenuation curves with those in Fig. 3, we find that the effects of increasing crack fluid viscosity are equivalent to those of decreasing crack permeability. This is due to the fact that the dispersion and attenuation are essentially determined by the fluid mobility (the ratio of crack permeability to fluid viscosity).

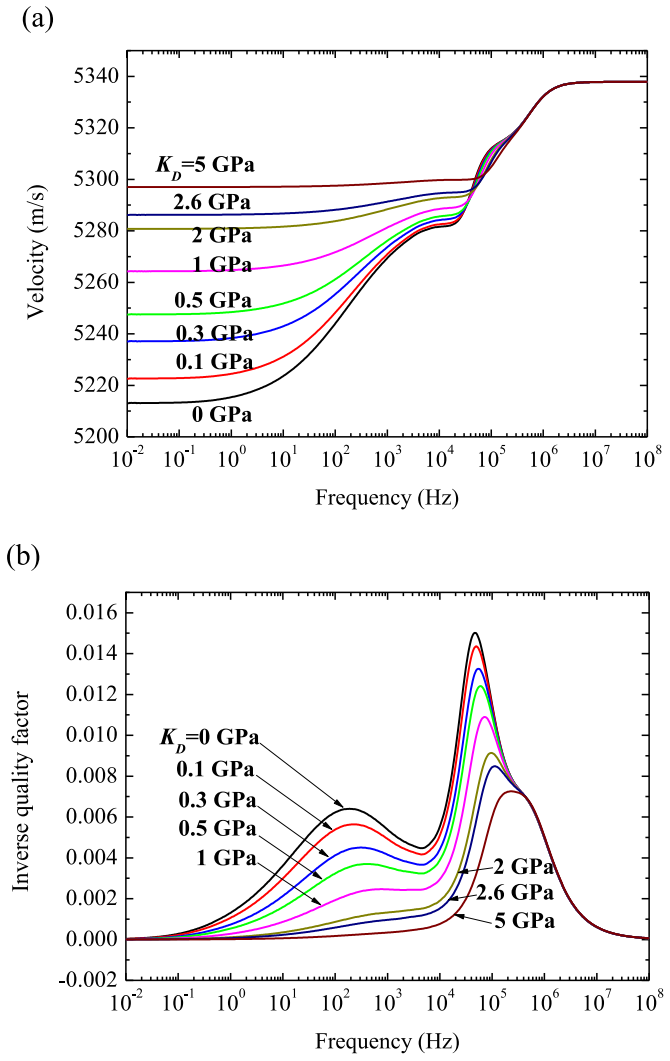

Fig. 5. P-wave phase velocity (a) and inverse quality factor (b) versus frequency for different crack frame bulk moduli.

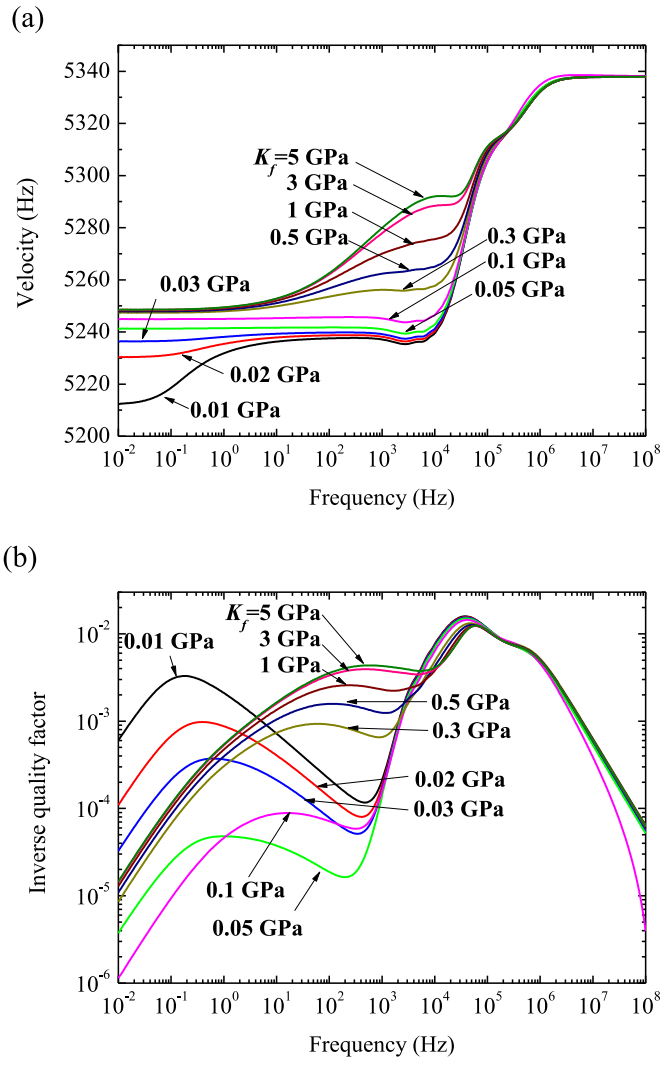

Fig. 6. P-wave phase velocity (a) and inverse quality factor (b) versus frequency for different crack fluid bulk moduli.

4.3. Effects of crack frame bulk modulus on wave dispersion and attenuation

It is interesting to investigate the effects of crack frame bulk modulus K_D on wave dispersion and attenuation because strong scattering can be produced by compliant cracks. The frame bulk modulus is one of basic parameters for porous media and it can be related to the undrained bulk modulus $K_U (=H_U - \frac{4}{3}\mu)$ via Gassmann's (1951) equation $K_U = K_D + \alpha^2 M$, where the definitions of α (Biot-Willis coefficient) and M (storage modulus) have been clarified in Section 2.1. In Fig. 5, we plot P-wave velocity and inverse quality factor versus frequency for different crack frame bulk moduli. In Fig. 5(a), it is shown that the total dispersion magnitude (the velocity difference between high- and low-frequency limits) and attenuation decrease with the increase of the crack frame bulk modulus. The P-wave velocity increases with the crack frame bulk modulus in the low-frequency range (WIFF-dominated frequency range), but it decreases with the crack frame bulk modulus in the intermediate-frequency range (elastic scattering-dominated frequency range).

Fig. 5(b) shows that both of the attenuation due to WIFF and the attenuation due to elastic scattering decrease with the crack frame bulk modulus. These results agree with our expectation because of that the more compliance the crack is, the stronger scattering can be caused by the crack. Moreover, the characteristic frequency of elastic scattering shifts toward higher frequencies with the increase of the crack frame bulk modulus. The reason is most likely that, at a given frequency the characteristic wavelength increases with the crack frame bulk modulus so that the characteristic frequency of the elastic scattering increases.

4.4. Effects of crack fluid bulk modulus on wave dispersion and attenuation

It has been widely recognized that the rocks are often filled with multi-phase fluids. It is of interest to explore how the multi-phase fluids affect the seismic waves in cracked rocks. Aside from the fluid viscosity effects studied in Fig. 4, the crack fluid compressibility can also significantly affect the velocity dispersion and attenuation. Thus, Fig. 6 depicts P-wave phase velocity (a) and inverse quality factor (b) versus frequency for different values of the crack fluid bulk modulus K_f. Fig. 6(a) shows that the general trend in velocity is that the total magnitude of the velocity dispersion increases with the decrease of K_f. In Fig. 6(a), we can observe three different dispersion portions in different frequency ranges. The first (low-frequency) dispersion occurs within the frequency band $f < 10^4$ Hz and it corresponds to the contribution of WIFF. The second (intermediate-frequency) dispersion roughly occurs at frequencies $10^4 < f < 2 \times 10^5$ Hz and it is caused by elastic scattering. The third (high-frequency) dispersion takes place in the frequency range $f > 2 \times 10^5$ Hz and it is owing to Biot's global flow.

It can be seen that for different crack bulk moduli, significant

differences in velocity and attenuation occur in the low-frequency range (WIFF-dominated frequency range). As K_f decreases, the WIFF-dominated dispersion magnitude (the velocity change within the WIFF-dominated frequency range) first decreases, and then conversely increases. A similar phenomenon was observed by Kong et al. (2013) in a periodic system of two different porous layers and can be explained as below. For the case of large value of crack fluid bulk modulus, during each oscillatory compressional half-cycle, high fluid pressure will be induced in the crack so that the fluid will flow into the matrix. In contrast, for the case of small value of crack fluid bulk modulus, the induced fluid pressure in the crack is smaller than that in the matrix pores. In this second case, the fluid will conversely flow into the crack. Therefore, there must be an intermediate case in which no flow occurs between the cracks and micro-scale pores. In this particular case, the dispersion due to WIFF disappears.

Another result that can be found in Fig. 6(b) is that the characteristic frequency of the WIFF moves to lower frequencies when K_f decreases. This result is expected, since the crack diffusivity is roughly proportional to the crack fluid bulk modulus. If the diffusivity decreases, the fluid will need more time to flow across the crack.

Furthermore, the dispersion magnitude and attenuation due to elastic scattering monotonously increases with the decrease of K_f (the increase of crack fluid compressibility). This is because of that the no-flow-limit velocity decreases with the increase of the crack fluid compressibility, resulting in stronger elastic scattering.

4.5. Effects of crack size on wave dispersion and attenuation

To study the dependence of characteristics of the dispersion and attenuation on crack sizes, Fig. 7 shows the P-wave velocity and inverse quality factor as functions of frequency for six different values of the crack radius. In Fig. 7, we keep the crack aspect ratio and the crack density unchanged. We see that all velocity curves converge to the same value in the low-frequency limit, demonstrating that the low-frequency velocity is determined by the crack density. This result agrees with previous works (e.g., Budiansky and O'Connell, 1976; Benveniste, 1987) that for an elastic non-porous matrix with a distribution of dry cracks, the low-frequency effective velocity is determined by the crack density rather than the crack volume fraction. We also see that when the crack size increases by one order of magnitude, the characteristic frequency of the WIFF shifts to low-frequency range by two orders of magnitude, while the characteristic frequency of the elastic scattering shifts to low frequency-range by only one order of magnitude. These results are expected, since the characteristic frequency of the WIFF is proportional to the inverse square of the crack radius (Müller et al., 2010; Galvin and Gurevich, 2015) (or the characteristic frequency of the WIFF is proportional to the inverse of the area of the crack interface), while the characteristic frequency of the elastic scattering is proportional to the inverse of the crack radius.

4.6. Comparison with the incompressible-fluid-crack model

In the last example, we aim at comparing the present effective medium model with a previous incompressible-fluid-crack model. Galvin and Gurevich (2007, 2009) first solved the problem of scattering by a crack containing incompressible fluid and developed an effective medium model for porous medium permeated by a random distribution of aligned cracks. Because they focused on the dispersion and attenuation in low-frequency range, their model is developed based on a kind of simplified Biot's theory in which Biot's global flow is ignored. Song et al. (2017a) and Song (2017) rederived the solution of such scattering problem by using the full framework of Biot's theory.

In order to examine the effects of fluid motion inside the crack on wave dispersion and attenuation, in Fig. 8 we compare the present model with Song's (2017) work for different crack permeability coefficients. For this example, in addition to the properties shown in

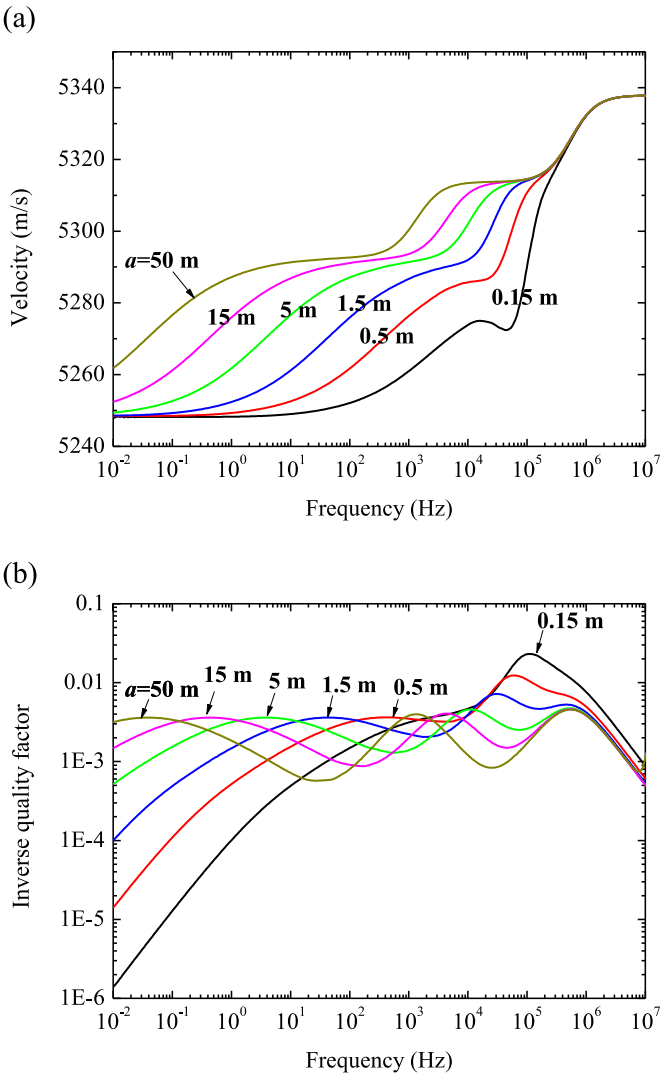

Fig. 7. P-wave phase velocity (a) and inverse quality factor (b) versus frequency for different crack sizes.

Table 1, we assume that the crack frame bulk and shear moduli $K_D = 0.001K_D^B$ and $\mu = 0.001\mu^B$, where K_D^B and μ^B are the matrix frame bulk and shear moduli.

Analogously to Fig. 3, we find that for low crack permeability (here, $k_0 < 10^{-16}\text{m}^2$) the dispersion characteristic frequency (i.e., the frequency at which the velocity changes the most strongest) of the WIFF is sensitive to the crack permeability, whereas for high crack permeability ($k_0 > 10^{-16}\text{m}^2$) the effects of crack permeability on dispersion and attenuation are negligible. It is worthy to mention that the characteristic frequencies at high crack permeability coefficients are close to that of the incompressible-crack-fluid model. This result indicates that the incompressible-crack-fluid model assumes its crack permeability value to be very large.

By comparing the curves with those in Fig. 3 in which the crack stiffnesses are greater than those in Fig. 8, we can verify the crack elastic properties can not only largely determine the velocity but also significantly change the characteristic frequency of the WIFF. This is due to the fact that apart from the fluid mobility, the crack elastic properties also control the crack hydraulic diffusivity which is a key parameter for determining the flow pattern.

5. Conclusions

Mechanical and hydraulic properties of the cracks have been shown

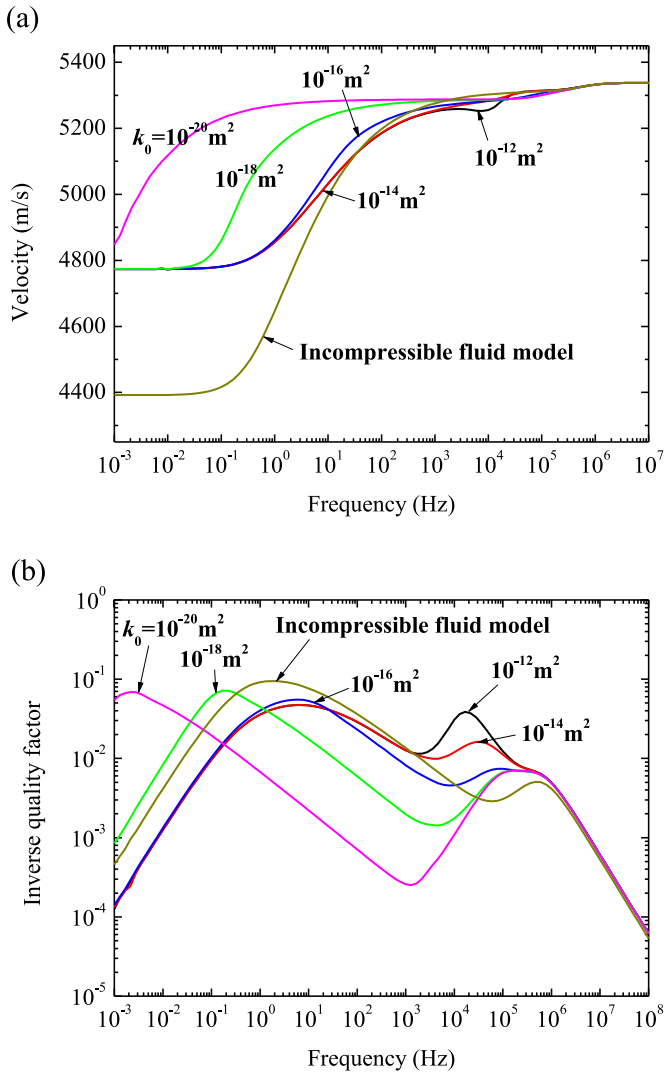

Fig. 8. Comparison of the P-wave velocity and inverse quality factor between the present model and previous incompressible-crack-fluid model. .

to have significant impacts on seismic signatures of cracked rocks. We have studied the effective properties of fluid-saturated porous rocks with aligned cracks containing compressible infillings which have different poroelastic properties from the background materials. To do so, we first solved the elastic wave scattering problem of an incident P wave by a circular crack. In particular, to study the effects of mechanical and hydraulic properties of the crack on the scattering, we used poroelastic linear slip conditions to describe the relations between crack properties and the stress and displacement discontinuities across the crack. Then, based on the exact scattering solutions we estimated attenuation and dispersion of elastic waves in rocks with a sparse distribution of aligned cracks by using Foldy's method. We also showed how the present model reduces to previous model of crack containing incompressible fluid. In numerical examples, we explore the effects of mobility of the crack fluid, crack mechanical properties, crack fluid compressibility and crack size on velocity dispersion and attenuation. The significant findings and remarks are summarized as follows:

(1) We have considered three important attenuation mechanisms in the present model. The low-frequency attenuation is attributed to WIFF, the intermediate-frequency attenuation is caused by elastic scattering, while the high-frequency attenuation is caused by Biot's global flow. The first two attenuation peaks are sensitive to crack fluid mobility, crack elasticity, crack fluid compressibility and crack size.

(2) We find that the crack fluid mobility can largely control fluid flow and pore pressure distribution inside the crack and further affects the velocity dispersion and attenuation. For low crack fluid mobility, if it decreases by one order of magnitude the curves of the velocity dispersion and attenuation of WIFF will shift towards to low-frequency range by one order of magnitude. When the crack fluid mobility is comparable to or greater than that of the matrix, the dispersion and attenuation due to WIFF are no longer sensitive to the crack fluid mobility.

(3) We verified that the effects of crack frame bulk modulus on wave dispersion and attenuation are also important because strong scattering can be produced by compliant cracks. It is found that the total dispersion magnitude (the velocity difference between high- and low-frequency limits) and attenuation decrease with the increase of the crack frame bulk modulus. The P-wave velocity increases with the crack frame bulk modulus in the low-frequency range (WIFF-dominated frequency range), while it decreases with the crack frame bulk modulus in the intermediate-frequency range (elastic scattering-dominated frequency range).

(4) The crack fluid compressibility also plays an important role in controlling the dispersion magnitude and attenuation peak as well as dispersion characteristic frequencies at both low- and high-frequency ranges. The general trend in velocity is that the magnitude of velocity dispersion (the velocity difference between high-frequency and low-frequency limits) increases with the decrease of K_f. As K_f decreases, the magnitude of dispersion due to WIFF first decreases, and then conversely increases. A similar phenomenon is also observed by Kong et al. (2013) in a periodic system of two different porous layers. The characteristic frequency of WIFF moves to low-frequency range when K_f decreases. Moreover, we find that the magnitude of dispersion and attenuation due to elastic scattering monotonously increases with the decrease of K_f.

(5) We see that when the crack size increases by one order of magnitude the characteristic frequency of the WIFF shifts to low-frequency range by two orders of magnitude, while the characteristic frequency of the elastic scattering shifts to low-frequency range by only one order of magnitude.

In brevity, the present model extends a previous model and the above results allow us better interpret frequency-dependent effective P-wave velocity and attenuation in saturated-filled cracked rocks.

The present model assumes that the crack distribution is dilute, interactions between the multiple cracks will be analyzed in a separate paper.

Declaration of Competing Interest

None.

Acknowledgments

The authors thank three anonymous reviewers and the Editor-In-Chief Benjamin Loret for their helpful comments and constructive suggestions. This work was supported by the National Natural Science Foundation of China (Grant Nos. 11802074, 11734017, 41874129, 41974136 and 11871180), National Postdoctoral Program for Innovation Talents (Grant No. BX201700066), the China Postdoctoral Science Foundation (Grant No. 2018M630345) and the Fundamental Research Funds for the Central Universities (Grant No. HIT. NSRIF. 2020016). Yongjia Song would like to thank Dongmei Song and Junfeng Li for helping him find some old but quite relevant articles from the National Library of China on their weekends.

Appendix A. Expressions of several functions

In this appendix, we collect expressions for functions $f_j^i(k)$ and s_j ($j = 1, 2, ...,4$).

$$f_1^i(k) = \frac{k_s^2 + 2\mu^B\eta_{N_D}[1-\alpha\tilde{B}(1-\Pi)]k^2\eta_s}{2k^2 - k_s^2}\eta_i - \frac{\mu^B\eta_{N_D}}{2}\{\alpha\Pi\varsigma_i^B k_i^2 + [1-\alpha\tilde{B}(1-\Pi)](2k^2 - \tau_i^B k_i^2)\}, \tag{A1}$$

$$f_2^i(k) = \left(\frac{2\chi_s^B k^2}{2k^2 - k_s^2} - \chi_i^B - \frac{2\alpha\eta_{N_D}\Pi\mu^B k^2\eta_s}{2k^2 - k_s^2}\right)\eta_i + \alpha\mu^B\eta_{N_D}\Pi\left(k^2 - \frac{\tau_i^B k_i^2}{2} + \frac{\varsigma_i^B k_i^2}{2\tilde{B}}\right), \tag{A2}$$

$$f_3^i(k) = -\frac{\tau_i^B k_i^2}{2k} - \eta_T\mu^B k\eta_i + \frac{\eta_T\mu^B}{4\eta_s k}(2k^2 - k_s^2)(2k^2 - \tau_i^B k_i^2), \tag{A3}$$

$$f_4^i(k) = -\mu^B\varsigma_i^B k_i^2 + \frac{1}{2}\frac{i\omega\eta_f}{\hat{\kappa}(\omega)}\Pi\frac{\chi_s^B}{2\eta_s}(2k^2 - \tau_i^B k_i^2) - \frac{1}{2}\frac{i\omega\eta_f}{\hat{\kappa}(\omega)}\Pi\chi_i^B\eta_i, \tag{A4}$$

$$s_1 = \eta_{N_D}[1-\alpha\tilde{B}(1-\Pi)]\sigma_{zz}^{in}|_{z=0} + \alpha\eta_{N_D}\Pi p^{in}|_{z=0}, \tag{A5}$$

$$s_2 = -\alpha\eta_{N_D}\Pi\sigma_{zz}^{in}|_{z=0} - \alpha\eta_{N_D}\Pi\frac{1}{\tilde{B}}p^{in}|_{z=0}, \tag{A6}$$

$$s_3 = \eta_T\sigma_{rz}^{in}|_{z=0}, \tag{A7}$$

$$s_4 = -\frac{i\omega\eta_f}{\hat{\kappa}(\omega)}\Pi w_z^{in}|_{z=0}. \tag{A8}$$

The expression of $f_j^i(k)$ ($j = 1, 2, ...,4$) is a function of the crack parameters and it serves as several intermediate functions for solving the integral equations, while s_j ($j = 1, 2, ...,4$) depends on the incident wave properties and it serves as the "source term" of the scattered waves.

Appendix B. Coefficients for the linear system of equations

In Section 2, we have showed that the integral equations of the scattering problem can be reduced to a linear system of equations. Now, detailed expressions of the coefficients in the linear system of equations are given in this appendix. The matrices given in Eq. (54) are

$$A_{lj} = \frac{\pi}{4}\frac{\Gamma(l+j+1)}{\Gamma(l-j+1.5)\Gamma(l+j+3)\Gamma(j-l+1.5)} + \mu^B\eta_{N_D}\int_0^\infty\left\{4[1-\alpha\tilde{B}(1-\Pi)]\frac{k^2\eta_s}{k_s^2}\right.$$
$$- \frac{2k^2\left(\chi_s^B - \chi_{ps}^B\right) + k_s^2\chi_{ps}^B}{k_s^2\left(\chi_{pf}^B - \chi_{ps}^B\right)\eta_{pf}}\left(\alpha\Pi\varsigma_{pf}^B k_{pf}^2 + [1-\alpha\tilde{B}(1-\Pi)](2k^2 - \tau_{pf}^B k_{pf}^2)\right)$$
$$\left. + \frac{2k^2\left(\chi_s^B - \chi_{pf}^B\right) + k_s^2\chi_{pf}^B}{k_s^2\left(\chi_{pf}^B - \chi_{ps}^B\right)\eta_{ps}}\left(\alpha\Pi\varsigma_{ps}^B k_{ps}^2 + [1-\alpha\tilde{B}(1-\Pi)](2k^2 - \tau_{ps}^B k_{ps}^2)\right)\right\}\frac{1}{k}j_{2l+1}(ka)j_{2j+1}(ka)\mathrm{d}k, \tag{B1}$$

$$B_{lj} = \mu^B\eta_{N_D}\int_0^\infty\left\{\frac{\alpha\Pi\varsigma_{pf}^B k_{pf}^2 + [1-\alpha\tilde{B}(1-\Pi)]\left(2k^2 - \tau_{pf}^B k_{pf}^2\right)}{\left(\chi_{pf}^B - \chi_{ps}^B\right)\eta_{pf}}\right.$$
$$\left. - \frac{\alpha\Pi\varsigma_{ps}^B k_{ps}^2 + [1-\alpha\tilde{B}(1-\Pi)](2k^2 - \tau_{ps}^B k_{ps}^2)}{\left(\chi_{pf}^B - \chi_{ps}^B\right)\eta_{ps}}\right\}\frac{1}{k}j_{2l+1}(ka)j_{2j+1}(ka)\mathrm{d}k, \tag{B2}$$

$$C_{lj} = \alpha\eta_{N_D}\Pi\mu^B\int_0^\infty\left[-\frac{4k^2\eta_s}{k_s^2} + \frac{2k^2\left(\chi_s^B - \chi_{ps}^B\right) + k_s^2\chi_{ps}^B}{k_s^2\left(\chi_{pf}^B - \chi_{ps}^B\right)\eta_{pf}}\left(2k^2 - \tau_{pf}^B k_{pf}^2 + \frac{\varsigma_{pf}^B}{\tilde{B}}k_{pf}^2\right)\right.$$
$$\left. - \frac{2k^2\left(\chi_s^B - \chi_{pf}^B\right) + k_s^2\chi_{pf}^B}{k_s^2\left(\chi_{pf}^B - \chi_{ps}^B\right)\eta_{ps}}\left(2k^2 - \tau_{ps}^B k_{ps}^2 + \frac{\varsigma_{ps}^B}{\tilde{B}}k_{ps}^2\right)\right]\frac{1}{k}j_{2l+1}(ka)j_{2j+1}(ka)\mathrm{d}k, \tag{B3}$$

$$D_{lj} = \frac{\pi}{4}\frac{\Gamma(l+j+1)}{\Gamma(l-j+1.5)\Gamma(l+j+3)\Gamma(j-l+1.5)}$$
$$-\frac{\alpha\mu^B\eta_{N_D}\Pi}{\chi^B_{pf}-\chi^B_{ps}}\int_0^\infty\left(\frac{2k^2-\tau^B_{pf}k^2_{pf}+\frac{\varsigma^B_{pf}}{\tilde{B}}k^2_{pf}}{\eta_{pf}}-\frac{2k^2-\tau^B_{ps}k^2_{ps}+\frac{\varsigma^B_{ps}}{\tilde{B}}k^2_{ps}}{\eta_{ps}}\right)\frac{1}{k}j_{2l+1}(ka)j_{2j+1}(ka)\mathrm{d}k, \tag{B4}$$

$$E_{lj} = \frac{\pi}{4}\frac{\Gamma(l+j+2)}{\Gamma(l-j+1.5)\Gamma(l+j+4)\Gamma(j-l+1.5)}$$
$$+\eta_T\mu^B\int_0^\infty\left\{\frac{2k^2-k_s^2}{\eta_s}\left[1+\frac{2k^2\left(\varsigma^B_{ps}k^2_{ps}-\varsigma^B_{pf}k^2_{pf}\right)}{\left(\tau^B_{ps}\varsigma^B_{pf}-\tau^B_{pf}\varsigma^B_{ps}\right)k^2_{pf}k^2_{ps}}\right]\right.$$
$$\left.-\frac{4\varsigma^B_{ps}k^2\eta_{pf}}{\left(\tau^B_{ps}\varsigma^B_{pf}-\tau^B_{pf}\varsigma^B_{ps}\right)k^2_{pf}}+\frac{4\varsigma^B_{pf}k^2\eta_{ps}}{\left(\tau^B_{ps}\varsigma^B_{pf}-\tau^B_{pf}\varsigma^B_{ps}\right)k^2_{ps}}\right\}\frac{1}{k}j_{2l+2}(ka)j_{2j+2}(ka)\mathrm{d}k, \tag{B5}$$

$$F_{lj} = \frac{\eta_T\mu^B}{a}\int_0^\infty\left[-\frac{2\tau^B_{ps}\eta_{pf}}{\left(\tau^B_{ps}\varsigma^B_{pf}-\tau^B_{pf}\varsigma^B_{ps}\right)k^2_{pf}}+\frac{2\tau^B_{pf}\eta_{ps}}{\left(\tau^B_{ps}\varsigma^B_{pf}-\tau^B_{pf}\varsigma^B_{ps}\right)k^2_{ps}}\right.$$
$$\left.+\frac{2k^2-k_s^2}{\eta_s}\frac{\left(\tau^B_{ps}k^2_{ps}-\tau^B_{pf}k^2_{pf}\right)}{\left(\tau^B_{ps}\varsigma^B_{pf}-\tau^B_{pf}\varsigma^B_{ps}\right)k^2_{pf}k^2_{ps}}\right]j_{2l+1}(ka)j_{2j+2}(ka)\mathrm{d}k, \tag{B6}$$

$$G_{lj} = \frac{\mathrm{i}\omega\eta_f\Pi a}{\mu^B\hat{k}(\omega)}\int_0^\infty\left\{\frac{\chi^B_s}{\eta_s}\left[1+\frac{2k^2\left(\varsigma^B_{ps}k^2_{ps}-\varsigma^B_{pf}k^2_{pf}\right)}{\left(\tau^B_{ps}\varsigma^B_{pf}-\tau^B_{pf}\varsigma^B_{ps}\right)k^2_{pf}k^2_{ps}}\right]-\frac{2\varsigma^B_{ps}k^2_{ps}\chi^B_{pf}\eta_{pf}-2\varsigma^B_{pf}k^2_{pf}\chi^B_{ps}\eta_{ps}}{\left(\tau^B_{ps}\varsigma^B_{pf}-\tau^B_{pf}\varsigma^B_{ps}\right)k^2_{pf}k^2_{ps}}\right\}j_{2l+2}(ka)j_{2j+1}(ka)\mathrm{d}k, \tag{B7}$$

$$H_{lj} = -\frac{\pi}{4}\frac{\Gamma(l+j+1)}{\Gamma(l-j+1.5)\Gamma(l+j+3)\Gamma(j-l+1.5)}$$
$$+\frac{\mathrm{i}\omega\eta_f\Pi}{\mu^B\hat{k}(\omega)}\int_0^\infty\frac{\frac{k^2}{\eta_s}\chi^B_s\left(\tau^B_{ps}k^2_{ps}-\tau^B_{pf}k^2_{pf}\right)-\chi^B_{pf}\tau^B_{ps}k^2_{ps}\eta_{pf}+\chi^B_{ps}\tau^B_{pf}k^2_{pf}\eta_{ps}}{\left(\varsigma^B_{pf}\tau^B_{ps}-\tau^B_{pf}\varsigma^B_{ps}\right)k^2_{ps}k^2_{pf}k}j_{2l+1}(ka)j_{2j+1}(ka)\mathrm{d}k, \tag{B8}$$

where $\Gamma()$ denotes the Gamma function.

The expansion coefficients for the incident wave are

$$\begin{cases}S^1_j = \frac{\mu^B\eta_{N_D}}{a}\left\{[1-\alpha\tilde{B}(1-\Pi)]\tau^B_{pf}-\alpha\Pi\varsigma^B_{pf}\right\}u_0\mathrm{i}k_{pf}\frac{\delta_{j0}}{3}\\ S^2_j = -\frac{\alpha\mu^B\eta_{N_D}\Pi}{a}\left(\tau^B_{pf}-\frac{\varsigma^B_{pf}}{\tilde{B}}\right)u_0\mathrm{i}k_{pf}\frac{\delta_{j0}}{3}\\ S^3_j = 0\\ S^4_j = -\frac{\mathrm{i}\omega\eta_f\Pi}{\mu^B\hat{k}(\omega)}u_0\chi_{pf}\frac{\delta_{j0}}{3}\end{cases}. \tag{B9}$$

References

Barbosa, N.D., Rubino, J.G., Caspari, E., Milani, M., Holliger, K., 2016. Fluid pressure diffusion effects on the seismic reflectivity of a single fracture. J. Acoust. Soc. Am. 140 (4), 2554–2570.

Barbosa, N.D., Rubino, J.G., Caspari, E., Milani, M., Holliger, K., 2017. Extension of the classical linear slip model for fluid-saturated fractures: accounting for fluid pressure diffusion effects. J. Geophys. Res. Solid Earth 122 (2), 1302–1323.

Batzle, M.L., Han, D.-H., Hofmann, R., 2006. Fluid mobility and frequency-dependent seismic velocity-direct measurements. Geophysics 71 (1), N1–N9.

Benveniste, Y., 1987. A new approach to the application of Mori-Tanaka's theory in composite materials. Mech. Mater. 6, 147–157.

Biot, M.A., 1962. Mechanics of deformation and acoustic propagation in porous media. J. Appl. Phys. 33, 1482–1498.

Bleistein, N., Handelsman, R.A., 1986. Asymptotic Expansions of Integrals. Dover Publications, New York.

Brajanovski, M., Gurevich, B., Schoenberg, M., 2005. A model for P-wave attenuation and dispersion in a porous medium permeated by aligned fractures. Geophys. J. Int. 163, 372–384.

Brajanovski, M., Müller, T.M., Gurevich, B., 2006. Characteristic frequencies of seismic attenuation due to wave-induced fluid flow in fractured porous media. Geophys. J. Int. 166, 574–578.

Budiansky, B., O'Connell, R.J., 1976. Elastic moduli of a cracked solid. Int. J. Solids Struct. 12, 81–97.

Chapman, M., Maultzsch, S., Liu, E., Li, X.-Y., 2003. The effect of fluid saturation in an anisotropic multi-scale equant porosity model. J. Appl. Geophys. 54, 191–202.

Chapman, M., 2003. Frequency-dependent anisotropy due to meso-scale fractures in the presence of equant porosity. Geophys. Prospect. 51, 369–379.

Deresiewicz, H.A., Skalak, R., 1963. On uniqueness in dynamic poroelasticity. Bull. Seismol. Soc. Am. 53, 783–788.

Eshelby, J.D., 1957. The determination of the elastic field of an ellipsoidal inclusion, and related problems. Proc. R. Soc. Lond. A: Math. Phys. Eng. Sci. 241, 376–396.

Foldy, L.L., 1945. The multiple scattering of waves. I. general theory of isotropic scattering by randomly distributed scatters. Phys. Rev. 67, 109–119.

Fu, B.-Y., Guo, J., Fu, L.-Y., Glubokovskikh, S., Galvin, R.J., Gurevich, B., 2018. Seismic dispersion and attenuation in saturated porous rock with aligned slit cracks. J. Geophys. Res. Solid Earth 123, 6890–6910.

Galvin, R.J., Gurevich, B., 2006. Interaction of an elastic wave with a circular crack in a fluid-saturated porous medium. Appl. Phys. Lett. 88, 061918.

Galvin, R.J., Gurevich, B., 2007. Scattering of a longitudinal wave by a circular crack fluid-saturated porous medium. Int. J. Solids Struct. 44, 7389–7398.

Galvin, R.J., Gurevich, B., 2009. Effective properties of a poroelastic medium containing a distribution of aligned cracks. J. Geophys. Res. 114, B07305.

Galvin, R.J., Gurevich, B., 2015. Frequency-dependent anisotropy of porous rocks with aligned fractures. Geophys. Prospect. 63, 141–150.
Gassmann, F., 1951. Uber die elasticität poröser medien (On the elasticity of porous media): vierteljahrsschrift der naturforschenden gesellschaft in Zürich. 96, 1–23.
Gubernatis, J.E., Domany, E., Krumhansl, J.A., 1977. Formal aspects of the theory of the scattering of ultrasound by flaws in elastic materials. J. Appl. Phys. 48, 2804–2811.
Guo, J., Rubino, G., Barbosa, N.D., Glubokovskikh, S., Gurevich, B., 2017a. Seismic dispersion and attenuation in saturated porous rocks with aligned fractures of finite thickness: theory and numerical simulations - Part 1: p-wave perpendicular to the fracture plane. Geophysics 83 (1), WA49–WA62.
Guo, J., Rubino, J.G., Barbosa, N.D., Glubokovskikh, S., Gurevich, B., 2017b. Seismic dispersion and attenuation in saturated porous rocks with aligned fractures of finite thickness: theory and numerical simulations - Part 2: frequency-dependent anisotropy. Geophysics 83 (1), WA63–WA71.
Guo, J., Shuai, D., Wei, J., Ding, P., Gurevich, B., 2018. P-wave dispersion and attenuation due to scattering by aligned fluid saturated fractures with finite thickness: theory and experiment. Geophys. J. Int. 215 (3), 2114–2133.
Gurevich, B., Brajanovski, M., Galvin, R.J., Müller, T.M., Toms-Stewart, J., 2009. P-wave dispersion and attenuation in fractured and porous reservoirs - poroelasticity approach. Geophys. Prospect. 57, 225–237.
Hudson, J.A., Liu, E., Crampin, S., 1996. The mechanical properties of materials with interconnected cracks and pores. Geophys. J. Int. 124, 105–112.
Hudson, J.A., 2000. The effect of fluid pressure on wave speeds in a cracked solid. Geophys. J. Int. 143, 302–310.
Johnson, D.L., Koplik, J., Dashen, R., 1987. Theory of dynamic permeability and tortuosity in fluid-saturated porous media. J. Fluid Mech. 1046 (176), 379–402.
Kawahara, J., Yamashita, T., 1992. Scattering of elastic waves by a fracture zone containing randomly distributed cracks. Pure Appl. Geophys. 139 (1), 121–144.
Kawahara, J., 1992. Scattering of P, sv waves by random distribution of aligned open cracks. J. Phys. Earth 40 (3), 517–524.
Kong, L., Gurevich, B., Müller, T.M., Wang, Y., Yang, H., 2013. Effect of fracture fill on seismic attenuation and dispersion in fractured porous rocks. Geophys. J. Int. 195, 1679–1688.
Kong, L., Gurevich, B., Zhang, Y., Wang, Y., 2017. Effect of fracture fill on frequency-dependent anisotropy of fractured porous rocks. Geophys. Prospect. 65 (6), 1649–1661.
Krenk, S., 1982. Some integral relations of Hankel transform type and applications to elasticity theory. Integral Equ. Oper. Theory 5, 548–561.
Krenk, S., Schmidt, H., 1982. Elastic wave scattering by a circular crack. Philos. Trans. R. Soc. Lond., Ser. A, Math. Phys. Sci. 308, 167–198.
Lambert, G., Gurevich, B., Brajanovski, M., 2006. Attenuation and dispersion of P-waves in porous rocks with planar fractures: comparison of theory and numerical simulations. Geophysics 71 (3), N41–N45.
Masson, Y.J., Pride, S.R., 2007. Poroelastic finite difference modelling of seismic attenuation and dispersion due to mesoscopic-scale heterogeneity. J. Geophys. Res. 112, B03204.
Maultzsch, S., Chapman, M., Liu, E., Li, X.Y., 2003. Modelling frequency-dependent seismic anisotropy in fluid-saturated rock with aligned fractures: implication of fracture size estimation from anisotropic measurements. Geophys. Prospect. 51, 381–392.
Maultzsch, S., Chapman, M., Liu, E., Li, X.-Y., 2007. Modelling and analysis of attenuation anisotropy in multi-azimuth VSP data from the Clair field. Geophys. Prospect. 55, 624–627.
Müller, T.M., Gurevich, B., Lebedev, M., 2010. Seismic wave attenuation and dispersion resulting from wave-induced flow in porous rocks – A review. Geophysics 75 (5), 75A147–75A164.
Nakagawa, S., Schoenberg, M.A., 2007. Poroelastic modeling of seismic boundary conditions across a fracture. J. Acoust. Soc. Am. 122 (2), 831–847.
O'Connell, R., Budiansky, B., 1977. Viscoelastic properties of fluid-saturated cracked solids. J. Geophys. Res. 82 (36), 5719–5735.
Olver, F.W.J., Lozier, D.W., Boisvert, R.F., Clark, C.W., 2010. NIST Handbook of Mathematical Functions. Cambridge University Press.
Pearce, R.G., Hudson, J.A., Douglas, A., 1988. On the use of P-wave seismograms to identify a double-couple source. Bull. Seismol. Soc. Am. 78 (2), 651–671.
Pointer, T., Liu, E., Hudson, J.A., 2000. Seismic wave propagation in cracked porous media. Geophys. J. Int. 142, 199–231.
Quintal, B., Jänicke, R., Rubino, J.G., Steeb, H., Holliger, K., 2014. Sensitivity of S-wave attenuation to the connectivity of fractures in fluid-saturated rocks. Geophysics 79, WB15–WB24.
Rubino, J.G., Guarracino, L., Müller, T.M., Holliger, K., 2013. Do seismic waves sense fracture connectivity? Geophys. Res. Lett. 40, 50127.
Rubino, J.G., Müller, T.M., Guarracino, L., Milani, M., Holliger, K., 2014. Seismioacoustic signatures of fracture connectivity. J. Geophys. Res. 119, 2252–2271.
Rubino, J.G., Castromán, G.A., Müller, T.M., Monachesi, L.B., Zyserman, F.I., Holliger, K., 2015. Including poroelastic effects in the linear slip theory. Geophysics 80 (2), A51–A56.
Rudnicki, J.W., 2013. 2011 Drucker medal paper: localized compaction in porous sandstones. J. Appl. Mech. 2013 (80), 061025.
Sayers, C.M., Kachanov, M., 1991. A simple technique for finding effective elastic constants of cracked solids for arbitrary crack orientation statistics. Int. J. Solids Struct. 27 (6), 671–680.
Sayers, C.M., Kachanov, M., 1995. Microcrack-induced elastic wave anisotropy of brittle rocks. J. Geophys. Res. 100 (B3), 4149–4156.
Schoenberg, M., Sayers, C.M., 1995. Seismic anisotropy of fractured rock. Geophysics 60, 204–211.
Smyshlyaev, V.P., Willis, J.R., Sabina, F.J., 1993. Self-consistent analysis of waves in a matrix-inclusion composite-III. a matrix containing cracks. J. Mech. Phys. Solids 41, 1809–1824.
Song, Y., Hu, H., Rudnicki, J.W., 2017a. Dynamic stress intensity factor (Mode I) of a permeable penny-shaped crack in a fluid-saturated poroelastic solid. Int. J. Solids Struct. 110–111, 127–136.
Song, Y., Hu, H., Rudnicki, J.W., 2017b. Normal compression wave scattering by a permeable crack in a fluid-saturated poroelastic solid. Acta Mech. Sin. 33, 356–367.
Song, Y., Hu, H., Bo, H., 2019. Elastic wave scattering by a fluid-saturated circular crack and effective properties of a solid with a sparse distribution of aligned cracks. J. Acoust. Soc. Am. 146 (1), 470–485.
Song, Y., 2017. Dynamic-equivalent model of heterogeneous porous medium and longitudinal wave scattering by a permeable crack in a porous medium. Harbin Institute of Technology, Harbin.
Worthington, M.H., Hudson, J.A., 2000. Fault properties from seismic Q. Geophys. J. Int. 143, 937–944.
Zhao, Y., Qiu, Y., Jacobs, L.J., Qu, J., 2015. Frequency-dependent tensile and compressive effective moduli of elastic solids with randomly distributed two-dimensional microcracks. J. Appl. Mech. 2015 (82), 081006.